Shock Waves (2018) 28:1285–1297
https://doi.org/10.1007/s00193-018-0848-7

ORIGINAL ARTICLE

Two-dimensional CFD–DEM simulation of vertical shock wave-induced dust lifting processes

K. Shimura[1] · **A. Matsuo**[1]

Received: 2 February 2018 / Revised: 17 May 2018 / Accepted: 25 June 2018 / Published online: 27 July 2018

Abstract

This paper conducts a numerical study of particle dispersion by vertical shock waves using a combination of computational fluid dynamics and the discrete element method (DEM). The Magnus force is important for particle dispersion, and the DEM approach can consider the rotation of individual particles and provide a detailed analysis of particle–particle and particle–wall interactions. Simulations are conducted and the results are compared with those of previous experiments, showing that the models can capture the particle dispersion process and shock wave geometry inside the mixed gas–particle region. During the particle dispersion process, the contact force due to the particle–particle interactions causes the particles to move upward after the shock wave passes and then decreases rapidly due to the low collision frequency in the particle cloud. The Magnus force is initially lower and has little effect until the contact force decreases, when it becomes dominant and maintains the particles' upward movement. It is mainly driven by the gas rotation above the dust layer, and the effect of particle rotation is relatively small in comparison. The gas velocity gradient above the dust layer in the particle dispersion region is caused by gas–particle interactions. The particle dispersion region becomes wider and thinner over time, meaning that the gas velocity gradient above the dust layer becomes small and hence that the Magnus force (which is driven by the gas rotation) also becomes small. In contrast, the downward drag force remains constant during the vertical motion because it is primarily affected by the velocity difference between the particles and the gas. This means that the drag and Magnus forces eventually balance, and the particles stop rising.

Keywords Computational fluid dynamics · Discrete element method · Gas/particle two-phase flow · Shock wave · Dust dispersion

1 Introduction

Granular materials can cause dust explosions in industrial facilities such as coal mines, food processing plants, and grain stores. Since the turn of the century, the number of dust explosion-related accidents has steadily increased despite improved safety procedures [1]. Gravity generally causes dust particles to form layers on the bottom surface, and they are unreactive when in bulk. Dust explosions thus only occur after the particles have been dispersed into the ambient air, and the primary explosion is typically triggered by frictional heat. Interactions between the primary shock wave and the layers of particles lift more dust, and the resulting suspended reactive particles cause secondary explosions when they are ignited by the shock-heated gas. These secondary explosions lead to further dust lifting and ignition, resulting in a sequence of explosions. Particle dispersion during the dust lifting process is therefore an important part of the dust explosion process.

The dust lifting process involves shock wave propagation, gas–particle interactions, and particle collisions. The essential factors and mechanisms underlying this complex physical process have been investigated both experimentally and numerically. Dawers [2], Gerrard [3], and Fletcher [4] conducted early investigations on the formation of dust clouds using shock tubes, and they observed experimentally that the layered particles' interactions caused curved shock

---

Communicated by A. Higgins.

✉ K. Shimura
shimura@mech.keio.ac.jp

A. Matsuo
matsuo@mech.keio.ac.jp

[1] Department of Mechanical Engineering, Keio University, 3-14-1 Hiyoshi, Kohoku-ku, Yokohama, Kanagawa 223-8522, Japan

waves. Suzuki [5] studied the particle motion and rotation in detail to understand the lifting mechanism. Chowdhury et al. [6] used Schlieren visualizations to clarify the dust dispersion process, and their experiments revealed that the lifting process involved two stages: an initial fast rising phase followed by a slower rising phase.

Two approaches have been taken to simulating dust dispersion numerically, namely Eulerian–Eulerian and Eulerian–Lagrangian methods, both of which treat the gas phase as a continuous fluid using an Eulerian approach. The Eulerian–Eulerian approach represents the discrete particles as a continuum, which allows relatively large-scale simulations to be conducted due to the low computational cost. However, this also means the particle–particle interactions cannot be described directly and must instead be inferred from the solid's pressure and viscosity using appropriate equations [7].

The kinetic theory for granular flow (KTGF) [8] is a state-of-the-art method of deriving equations for the solid's pressure without requiring an empirical formula. Recent numerical studies have used it to propose numerical procedures for the dust lifting problem and demonstrated their ability to simulate particle dispersion, including shock wave propagation and interaction [9–12]. Khmel et al. [12] also used the KTGF to conduct a numerical study, which led them to suggest that the Magnus force is much more significant than the Saffman force for the vertical movement of layered particles. Although both are lift forces, the Saffman force originates from the shear flows around particles, while the Magnus force is caused by particle rotation, and hence estimating it requires the rotation of individual particles to be tracked accurately. Unfortunately, the Eulerian–Eulerian approach is unable to track the rotation of individual particles and can only calculate the continuum fluid's vorticity in the solid phase.

The Eulerian–Lagrangian approach combines the Lagrangian method for discrete particles with the Eulerian method for continuous ambient fluids. This has the advantage that the particle–particle interactions are easy to calculate, but it is usually very computationally expensive. Two strategies can be used to calculate the gas–particle interactions: the resolved discrete particle model (RDPM) and the unresolved discrete particle model (UDPM) [7]. In the RDPM, the computational cells used for the gas phase are smaller than the particle diameter, and the gas–particle interactions are calculated using the boundary conditions at the particle surfaces. This is the most accurate method for studying gas–particle flows, but also the most computationally expensive, due to the fine grid required. In contrast, the UDPM uses computational cells that are larger than the particle diameter, and uses a drag force model to calculate the gas–particle interactions. To simulate the dust lifting problem with particles that are 10^{-5}–10^{-6} m in size, the RDPM would require a computational grid width of 10^{-6}–10^{-7} m, which is too computationally expensive. Thus, since the UDPM offers a more feasible calculation time, it will be used in this study.

This paper presents a UDPM-based two-dimensional computational fluid dynamics–discrete element method (CFD–DEM) procedure for calculating particle dispersions. In particular, the dust lifting problem, including shock wave–particle interactions, is studied to investigate the effect of the Magnus force on the lifting process. To validate the method, the chosen numerical target is similar to that used in a previous experimental study [5]. First, suitable parameters are determined for the particle collisions and Magnus force by comparing the calculated results with the experimental ones. Then, the effects of the forces acting on the particles are evaluated. Finally, a series of simulations is conducted to investigate the effect of the particle diameter on the lifting process.

2 Numerical method

In this study, the individual particles are assumed to be incompressible, and thus, the porosity $\alpha_g = 1 - \alpha_p$ is independent of the gas phase quantities, e.g., the gas pressure [8]. (Here, α_g is the particle phase volume fraction.) Note that the porosity is not constant and depends on the particle distribution. During the shock dispersion process, the particle layer deformation affects the gas phase due to the resulting particle movement.

The governing equation for the gas phase is essentially the same as in the well-known two-fluid models [13], although it also introduces the porosity. In the momentum equation, the pressure terms, $\nabla \alpha_g p_g - p_g \nabla \alpha_g$, can be simplified to just $\alpha_g \nabla p_g$ by assuming that the particles are incompressible. The gas phase is assumed to be a compressible viscous fluid with the same composition as air, namely an O_2:N_2 ratio of 1:3.76. The conservation laws for mass, momentum, and total energy can thus be expressed as follows.

$$\frac{\partial}{\partial t}\left(\alpha_g \rho_g\right) + \nabla \cdot \left(\alpha_g \rho_g \mathbf{u}_g\right) = 0 \tag{1}$$

$$\frac{\partial}{\partial t}\left(\alpha_g \rho_g \mathbf{u}_g\right) + \nabla \cdot \left(\alpha_g \rho_g \mathbf{u}_g \mathbf{u}_g\right) + \alpha_g \nabla p_g - \nabla \cdot \left(\alpha_g \boldsymbol{\tau}_g\right) = -\mathbf{f}_p \tag{2}$$

$$\frac{\partial}{\partial t}\left(\alpha_g e_g\right) + \nabla \cdot \left[\alpha_g \left(e_g + p_g\right) \mathbf{u}_g\right] - \nabla \cdot \left(\alpha_g \boldsymbol{\tau}_g \mathbf{u}_g\right) - \nabla \cdot \left(\alpha_g \mathbf{q}_g\right) = -p_g \frac{\partial}{\partial t} \alpha_g - s_p - q_p \tag{3}$$

Here, ρ_g, $\mathbf{u}_g$, p_g, $\boldsymbol{\tau}_g$, e_g, and $\mathbf{q}_g$ are the density, velocity vector, gas pressure, stress tensor, total energy, and heat flux, respectively. The source terms $\mathbf{f}_p$ and s_p are the momentum and energy exchanged by the aerodynamic forces, and q_p is the energy exchanged by heat transfer. The set of equations is completed by assuming the gas to be thermally perfect and using the ideal equation of state. The heat capacity and enthalpy can be estimated by using the NASA polynomials and taking the coefficients from the CETPC table [14], and the equation of state is

$$p_{\mathrm{g}} = \rho_{\mathrm{g}} R_{\mathrm{g}} T_{\mathrm{g}} \tag{4}$$

where R_{g} and T_{g} are the gas constant and gas temperature, respectively. The viscosity and thermal conductivity of the gas phase are calculated using the Gordon equation [15] with the Wilke combination rule to account for the temperature dependency.

The particle phase is treated as being discrete and described by the DEM with coarse graining. The individual particles are governed by the equations of motion for translation and rotation, and by conservation of energy, with their heat capacity assumed to be constant. Thus, the governing equations for particle i are as follows.

$$m_i \frac{\mathrm{d}\mathbf{u}_i}{\mathrm{d}t} = \sum_{\forall j \in \text{collision}} \mathbf{F}_{\text{contact},i,j} + \mathbf{F}_{\text{drag},i} + \mathbf{F}_{\text{Magnus},i} + \mathbf{F}_{\text{pressure},i} \tag{5}$$

$$I_i \frac{\mathrm{d}\boldsymbol{\omega}_i}{\mathrm{d}t} = \sum_{\forall j \in \text{collision}} \mathbf{M}_{\text{contact},i,j} + \mathbf{M}_{\text{rotation},i} \tag{6}$$

$$m_i c_i \frac{\mathrm{d}T_i}{\mathrm{d}t} = Q_i \tag{7}$$

Here, $m_i, \mathbf{u}_i, I_i, \boldsymbol{\omega}_i, c_i$, and T_i are the mass, translational velocity vector, moment of inertia, angular velocity vector, specific heat capacity, and surface temperature of particle i, respectively. In this two-dimensional simulation, $\boldsymbol{\omega}_i$ only has a component in the z-direction.

The forces acting on the particles include the particle–particle contact force $\mathbf{F}_{\text{contact}}$, viscous drag force $\mathbf{F}_{\text{drag}}$, Magnus force $\mathbf{F}_{\text{Magnus}}$, and pressure gradient force $\mathbf{F}_{\text{pressure}}$. The contact torque $\mathbf{M}_{\text{contact}}$ is generated by the tangential contact force, and $\mathbf{M}_{\text{rotation}}$ is generated by the viscous friction between particle i and the ambient gas. The equations used to calculate the individual-particle forces and torques appearing in (5, 6) are listed in Table 1.

The Saffman lift force is neglected in this study as it has little effect on the particle dispersion process [12]. The added mass force and Basset force are also neglected as they have only slight effects on compressible gas–particle flows [16]. The Magnus force coefficient C_{LM} is constant, and its value will be determined later, by the parameter study conducted in Sect. 3. Due to their low Biot numbers ($\text{Bi} \ll 1$), the particles' internal temperature gradients can be neglected, and their internal energies can be described in terms of their surface temperatures, specific heat capacities, and masses. Temperature increases due to viscoelastic effects caused by particle collisions are also neglected. The heat transfer Q_i represents only the heat transferred between particle i and the gas, as inter-particle radiation is neglected because the temperature differences between the particles are quite small. It is calculated as follows.

$$Q_i = S_i h_i \left(T_{\mathrm{g}} - T_i\right) \tag{8}$$

$$h_i = \frac{\mathrm{Nu}_i \kappa_{\mathrm{g}}}{d_i} \tag{9}$$

$$\mathrm{Nu}_i = 2 + 0.6\mathrm{Pr}_i^{1/3} + \mathrm{Re}_i^{1/2} \tag{10}$$

Here, S_i, d_i, and h_i are surface area, diameter, and local heat transfer coefficient for particle i, respectively, and κ_{g} is the thermal conductivity of the gas. The Ranz–Marshall equation [17] is used to estimate h_i.

This study uses more than 10^9 particles, so the computational cost of tracking them all individually would be prohibitive. Instead, the coarse graining model is used to reduce the computational cost by only tracking parcels. Sakai's method [23] is used to connect the DEM equations for the parcels with those for the real particles. The particles' translational motion is assumed to be the same as that of their parcels. Each parcel represents $n_i = n_{i,x} \times n_{i,y} \times n_{i,z} = n_{i,xy}^2 \times n_{i,z}$ particles, and its mass and diameter are n_i and $n_{i,xy}$ times that of a real particle, respectively. Here, $n_{i,x}$ and $n_{i,xy}$ are the numbers of particles in the parcel along the x-direction and similarly for $n_{i,y}$ and $n_{i,z}$. From the assumption relating the translational motions of parcels and real particles, the displacements between parcels are the same as those between particles, and the aerodynamic forces are n_i times larger than those acting on particles. The translational equation of motion and energy equation for parcels are therefore identical to those for real particles. Figure 1 illustrates the calculations for the aerodynamic and contact forces. The advantage of Sakai's method is that the real particles' properties can also be utilized for the parcels. This allows the contact forces and torques acting on individual particles to be calculated using the displacements between parcels, and the aerodynamic forces to be calculated using the real particles' physical properties. Note that $n_{i,xy} = n_{i,x} = n_{i,y} = d_{\text{parcel}}/d_{\text{RP}}$, while the $n_{i,z}$ are different because the simulations conducted in this study are two-dimensional. (Here, d_{parcel} and d_{RP} are the parcel and real particle displacements, respectively.) The parcels are cylindrical in shape.

In contrast, the procedure for estimating the parcels' moments of inertia is different from that for the mass. The relationship between the angular velocities of parcels and real particles is as follows.

Table 1 Equations for forces and torques acting on particle i

Force or torque	Symbols	Equations
Contact force	$\mathbf{F}_{\mathrm{contact},i,j}$	$\mathbf{F}_{\mathrm{contact},n,i,j} + \mathbf{F}_{\mathrm{contact},t,i,j}$
	$\mathbf{F}_{\mathrm{contact,n},i,j}$	$-k_{\mathrm{n}}\boldsymbol{\delta}_{\mathrm{n},ij} + h_{\mathrm{n}}\mathbf{u}_{\mathrm{n},ij}$
	$\mathbf{F}_{\mathrm{contact,t},i,j}$	$-k_{\mathrm{t}}\boldsymbol{\delta}_{\mathrm{t},ij} + h_{\mathrm{t}}\mathbf{u}_{\mathrm{t},ij}$
Drag force [18]	$\mathbf{F}_{\mathrm{drag},i}$	$3\pi\mu_{\mathrm{g}}d_i\mathbf{u}_{\mathrm{r},i}\frac{\mathrm{Re}_{\mathrm{p},i}}{24}\cdot C_{\mathrm{D,std}}\cdot\xi_1\left(M_{\mathrm{p},i},\mathrm{Re}_{\mathrm{p},i}\right)\cdot\xi_2\left(\alpha_{\mathrm{g}}\right)$
		$C_{\mathrm{D,std}} = \frac{24}{\mathrm{Re}_{\mathrm{p},i}}\left(1+0.15\mathrm{Re}_{\mathrm{p},i}\right)+0.42\left(1+\frac{42500}{\mathrm{Re}_{\mathrm{p},i}^{1}.16}\right)$
		$\xi_1\left(M_{\mathrm{p},i},\mathrm{Re}_{\mathrm{p},i}\right)$ and $\xi_2\left(\alpha_{\mathrm{g}}\right)$ can be found in Parmer et al. [19] and Sangani et al. [20]
Magnus force [21]	$\mathbf{F}_{\mathrm{Magnus},i}$	$\frac{1}{2}\rho_{\mathrm{g}}\mathbf{u}_{\mathrm{r},i}\lvert\mathbf{u}_{\mathrm{r},i}\rvert\frac{\pi d_i^2}{4}C_{\mathrm{LM}}\frac{d_i\lvert\boldsymbol{\omega}_{\mathrm{r},i}\rvert}{\lvert\mathbf{u}_{\mathrm{r},i}\rvert}\frac{\boldsymbol{\omega}_{\mathrm{r},i}\times\mathbf{u}_{\mathrm{r},i}}{\lvert\boldsymbol{\omega}_{\mathrm{r},i}\rvert\lvert\mathbf{u}_{\mathrm{r},i}\rvert}$
Pressure force	$\mathbf{F}_{\mathrm{pressure},i}$	$V_{\mathrm{p},i}\nabla p_{\mathrm{g}}$
Rolling torque	$\mathbf{M}_{\mathrm{contact},i}$	$\frac{d_i}{2}\mathbf{n}_{ij}\times\mathbf{F}_{\mathrm{contact,t},i,j}$
Frictional torque [22]	$\mathbf{M}_{\mathrm{rotation},i}$	$\frac{1}{64}C_{\mathrm{T}}d_i^5\rho_{\mathrm{g}}\boldsymbol{\omega}_{\mathrm{r},i}\lvert\boldsymbol{\omega}_{\mathrm{r},i}\rvert$
		$C_{\mathrm{T}} = \frac{6.45}{\sqrt{\mathrm{Re}_{\omega,i}}}+\frac{32.1}{\mathrm{Re}_{\omega,i}}$
$\mathbf{R}_{ij}$	Relative position vector from center of ith parcel to jth parcel	
$\mathbf{n}_{ij}$	Normal unit vector	$\mathbf{R}_{ij}/\lvert\mathbf{R}_{ij}\rvert$
$\boldsymbol{\delta}_{\mathrm{n},ij}$	Overlap	$\left[0.5\times\left(d_i+d_j\right)-\mathbf{R}_{ij}\cdot\mathbf{n}_{ij}\right]\mathbf{n}_{ij}$
$\boldsymbol{\delta}_{\mathrm{t},ij}$	Tangential displacement	$\int_{t_0}^{t}\mathbf{u}_{\mathrm{t},ij}dt$
$\mathbf{u}_{ij}$	Inter-particle relative velocity	$\mathbf{u}_j-\mathbf{u}_i-0.5\left(d_i\boldsymbol{\omega}_i+d_j\boldsymbol{\omega}_j\right)\times\mathbf{n}_{ij}$
		$\mathbf{u}_{\mathrm{n},ij}=\left(\mathbf{u}_{ij}\cdot\mathbf{n}_{ij}\right)\mathbf{n}_{ij},\ \mathbf{u}_{\mathrm{t},ij}=\mathbf{u}_{ij}-\mathbf{u}_{\mathrm{n},ij}$
$\mathbf{u}_{\mathrm{r},i}$	Gas–particle relative velocity	$\mathbf{u}_{\mathrm{g}}-\mathbf{u}_i$
$\boldsymbol{\omega}_{\mathrm{r},i}$	Relative angular velocity	$2\boldsymbol{\omega}_{\mathrm{g}}-\boldsymbol{\omega}_i$
$\mathrm{Re}_{\mathrm{p},i}$	Particle Reynolds number	$\rho_{\mathrm{g}}\lvert\mathbf{u}_{\mathrm{r},i}\rvert d_i/\mu_{\mathrm{g}}$
$\mathrm{Re}_{\omega,i}$	Spin Reynolds number	$0.25\lvert\boldsymbol{\omega}_{\mathrm{r},i}\rvert d_i^2\rho_{\mathrm{g}}/\mu_{\mathrm{g}}$

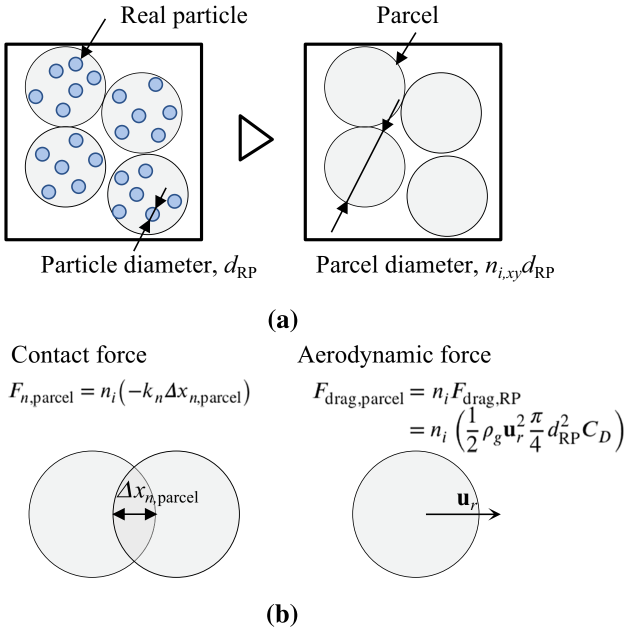

Fig. 1 Coarse graining illustration. The particle simulation only tracks parcels. The displacement between parcels is used to calculate the contact forces acting on particle. **a** Parcel configuration. **b** Force calculations under the coarse graining

$$\begin{aligned}\frac{\mathrm{d}\boldsymbol{\omega}_{\mathrm{parcel}}}{\mathrm{d}t} &= \frac{\mathbf{T}_{\mathrm{parcel}}}{I_{\mathrm{parcel}}} = \frac{\mathbf{r}_{\mathrm{parcel}}\times\mathbf{F}_{\mathrm{parcel}}}{\frac{1}{2}m_{\mathrm{parcel}}\cdot r_{\mathrm{parcel}}^2}\\ &= \frac{n_{i,xy}\mathbf{r}_{\mathrm{RP}}\times n_i\mathbf{F}_{\mathrm{RP}}}{\frac{1}{2}n_im_{\mathrm{RP}}\cdot n_{i,xy}^2r_{\mathrm{RP}}^2}\\ &= \frac{\mathbf{T}_{\mathrm{RP}}}{\frac{5}{4}n_{i,xy}I_{\mathrm{RP}}} = \frac{5}{4}\frac{1}{n_{i,xy}}\frac{\mathrm{d}\boldsymbol{\omega}_{\mathrm{RP}}}{\mathrm{d}t}\end{aligned} \tag{11}$$

Here, $\boldsymbol{\omega}_{\mathrm{parcel}}, r_{\mathrm{parcel}}, \mathbf{r}_{\mathrm{parcel}}, m_{\mathrm{parcel}}, \mathbf{T}_{\mathrm{parcel}}, \mathbf{F}_{\mathrm{parcel}}$, and I_{parcel} are the angular velocity, radius, vector from particle center to collision point, mass, torque, overall force, and moment of inertia for a parcel, and n_i is the number of real particles per parcel. The quantities subscripted by RP are the corresponding quantities for real particles. In summary, the coarse graining model uses (5–7) with the same physical properties as for real particles, while the moment of inertia and particle diameter are different. The number of real particles per parcel n_i mainly appears in the interphase exchange equations (12–15 below).

The governing equations for the gas phase (1–3) and the equations for individual particles (5–7) are coupled by the porosity α_g and the interphase exchange terms, $\mathbf{f}_p$, $\mathbf{s}_p$, and q_p. For each Eulerian cell, all interphase quantities are calculated by summing the contributions of each particle inside the cell, as follows.

$$\alpha_g = 1 - \alpha_p = 1 - \frac{1}{V_{cell}} \sum_{\forall_i \in cell} n_i V_i \tag{12}$$

$$\mathbf{f}_p = \frac{1}{V_{cell}} \sum_{\forall_i \in cell} n_i \left(\mathbf{F}_{drag,i} + \mathbf{F}_{Magnus,i} \right) \tag{13}$$

$$s_p = \frac{1}{V_{cell}} \sum_{\forall_i \in cell} n_i \left(\mathbf{F}_{drag,i} + \mathbf{F}_{Magnus,i} \right) \cdot \mathbf{u}_i \tag{14}$$

$$q_p = \frac{1}{V_{cell}} \sum_{\forall_i \in cell} n_i Q_i \tag{15}$$

Here, V_i is the volume of particle i and V_{cell} is the volume of each cell. Meanwhile, the gas phase quantities in (5–10) are calculated by interpolating the surrounding Eulerian cell values:

$$\xi_i = c_1 \xi_{j1,k1} + c_2 \xi_{j2,k1} + c_3 \xi_{j1,k2} + c_4 \xi_{j2,k2} \tag{16}$$

where c_{1-4} are the ratios of the areas of the triangles shown in Fig. 2 to the area of the entire cell and ξ_i is the quantity to be interpolated. The sum of the coefficients is normalized.

The governing equations' time evolution involves two components: particle and fluid calculations. The Courant–Friedrichs–Lewy (CFL) condition is used to estimate the size of the time steps needed for each calculation. Figure 3 shows the CFD–DEM simulation process as a flowchart. In this study, the time step for the particle calculations, Δt_{DEM}, was smaller than that for the fluid calculations, Δt_{CFD}, so the particle calculations were iterated for a period of Δt_{CFD} for each fluid calculation step. The time steps were estimated by the following equations using the Courant numbers ν_{CFD} and ν_{DEM}.

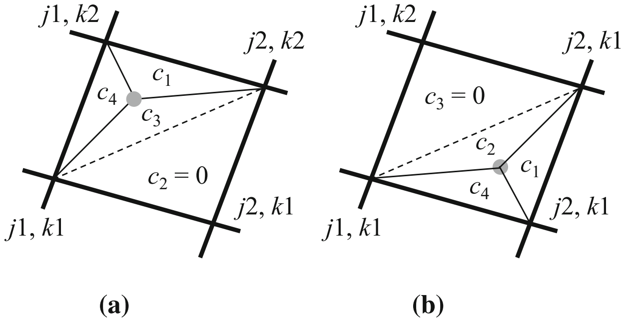

Fig. 2 Triangle-based weights used to interpolate the coefficients from cell to parcel. **a** Case 1. **b** Case 2

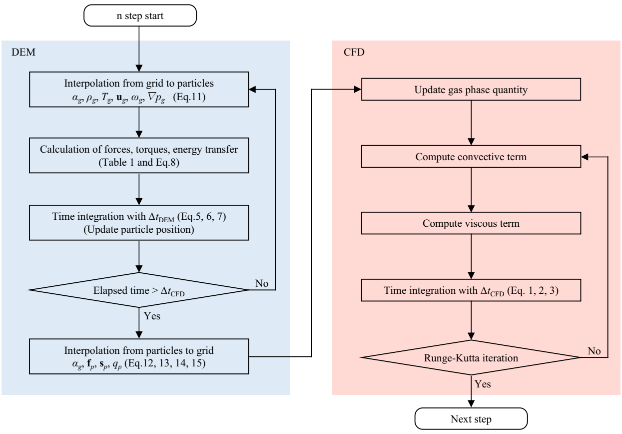

Fig. 3 CFD–DEM simulation flowchart

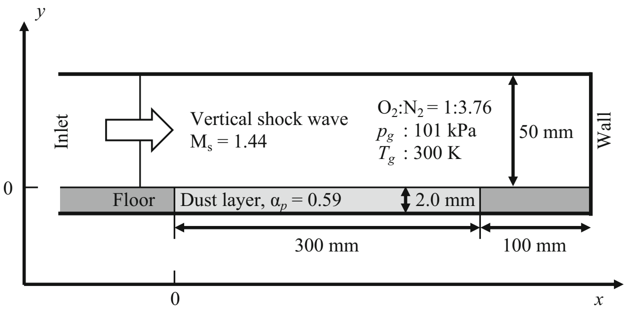

Fig. 4 Problem formulation for the interaction between a vertical shock wave and dust layer particles

$$\Delta t_{CFD} = \nu_{CFD} \frac{\Delta x}{\max \left(u_g + c_g, u_g - c_g \right)} \tag{17}$$

$$\Delta t_{DEM} = \nu_{DEM} \sqrt{\frac{m_i}{\max \left(k_n, k_t \right)}} \tag{18}$$

where c is speed of sound.

The fluid calculations were spatially discretized using third-order Simple Low Dissipation AUSM 2 (SLAU2) [24] with Monotonic Upwind Scheme for Conservation Laws (MUSCL) for the convection term and second-order central differencing for the viscous term, and the third-order total variation diminishing Runge–Kutta method [25] was used for time integration. The particle calculations used the first-order symplectic Euler method for time integration.

3 Result and discussion

3.1 Calculation conditions

Figure 4 illustrates the computational target for the particle dispersion analysis, which was similar to that used in previous experiments conducted by Suzuki et al. [5]. The main

Table 2 Parameters used for vertical shock problem calculations

Quantity	Value	Unit
Particle diameter	100	μm
Material density	980	kg/m^3
Heat capacity	1200	J/kg K
Dust layer volume fraction	0.59	–
Ambient gas pressure	101	kPa
Ambient gas temperature	300	K
Initial particle temperature	300	K
Shock wave Mach number	1.44	–
Domain of influence diameter	100	μm
Number of parcels	60,000	–
Minimum grid width	250	μm

computational region was a two-dimensional channel of size 400×52 mm, with a 400-mm upstream region added to prevent the shock waves being reflected at the left boundary. The minimum grid width was $\Delta x = \Delta y = 250\,\mu$m in the main region, and the computational grid was stretched vertically for $y > 32$ mm. The initial parameters used are listed in Table 2. A total of 1901×161 grid points and 60,000 parcels were used, and each parcel represented 90,000 real particles per meter in the z-direction.

3.2 Parameter selection via comparison with experiments

Parametric studies were conducted by comparing the output of the model with the experimental results to determine the spring constants k_{n} and k_{t}, damping constant h, and Magnus constant C_{LM}. (The same damping constant h was used for the tangential and normal directions). Figure 5 shows the horizontal dust layer surface distributions for different DEM parameters when the shock wave reached $x = 290$ mm ($t = 0.6$ ms). Here, the Magnus force was neglected and C_{LM} was set to 0. The dust layer's surface was found from the grid by first interpolating from the parcel distribution to the grid [see (12)] and then finding an interpolated value for α_{p} from the grid. This was done because the inter-parcel distance after shock dispersion was too large for the dust layer's surface to be defined smoothly, so the surface was instead defined as having a particle phase volume fraction of $\alpha_{\mathrm{p}} > 1.0 \times 10^{-4}$.

The size of the normal spring constant had no effect on the dust lifting height, as shown in Fig. 5a. In DEM-based structural analyses, the results converge for high normal spring constants, and these results indicate that CFD–DEM simulations converge similarly. According to (18), however, larger spring constants lead to smaller DEM time steps and higher computational costs, so the smallest value $k_{\mathrm{n}} = 50$ kN/m was used for subsequent simulations.

The dust lifting height was lower when $k_{\mathrm{n}}/k_{\mathrm{t}} > 0.02$, as shown in Fig. 5b. Since actual particles have much smaller spring constants in the tangential direction than in the normal direction, i.e., $k_{\mathrm{n}}/k_{\mathrm{t}} \ll 1$, these results are sufficient because larger $k_{\mathrm{n}}/k_{\mathrm{t}}$ ratios are unphysical. As a result, $k_{\mathrm{n}}/k_{\mathrm{t}} = 0.002$ was used for subsequent simulations.

Larger damping constants lead to lower lifting heights, as shown in Fig. 5c, because the particle phase kinetic energy is dissipated by viscoelastic effects caused by the particle collisions: the particles were only lifted by 1 mm for $h > 0.30$ mNs/m. In addition, the damping constant h affects the lifting delay distance, namely the distance between the shock wave and the point where dust lifting begins. When $h > 0.30$ mN s/m, the lifting delay distance was 100 mm, longer than the delay found experimentally. Thus, $h = 0.10$ mN s/m was used for subsequent calculations as it gave delay distances that agreed well with the experimental results.

Figure 6 shows the effect of different Magnus force coefficients C_{LM} on the dust lifting height. Values of $C_{\mathrm{LM}} = 0.10$–1.0 were tested, based on experimental observations of the movement of a single sphere [21,26,27]. Since the pressure and gravitational centers are different in practice, because actual dust particles are not spherical, the tested range included larger values than those found by the experiments to simulate easier initiation of particle rotation in the non-spherical case. According to Fig. 6, $C_{\mathrm{LM}} = 1.0$ gave the best agreement with the experimental results. Comparing the lifting heights at $x = 250$ mm shows a difference of about 1.0 mm between $C_{\mathrm{LM}} = 0.0$ and 1.0, meaning that the Magnus force has less effect than particle collisions. The lifting delay distance was the same in all cases. These results indicate that the lifting delay and initiation of dust lifting are not affected by the lift force but instead by particle collisions. Based on the above results, the DEM parameter values used were $k_{\mathrm{n}} = 50$ kN/m, $k_{\mathrm{n}}/k_{\mathrm{t}} = 0.002$, $h = 0.10$ mN s/m, and $C_{\mathrm{LM}} = 1.0$.

Figure 7 shows the effects of (a) the grid resolution and (b) the parcel diameter on the dust lifting height. Here, the parcel diameter used for the grid resolution study was $100\,\mu$m, and $\Delta x = 500\,\mu$m was used to investigate the effect of changing the parcel diameter. Figure 7a indicates that the dust layer's surface height converged for grid widths of $\Delta x = 500$ and $250\,\mu$m. However, Fig. 7b shows that large parcels lead to slightly higher particle lifting heights for $50 < x < 130$ mm. The trends in the dust layer's surface height are almost the same for parcel diameters of 100 and $200\,\mu$m. Based on these results, a grid width of $250\,\mu$m and a parcel diameter of $100\,\mu$m were used for subsequent simulations.

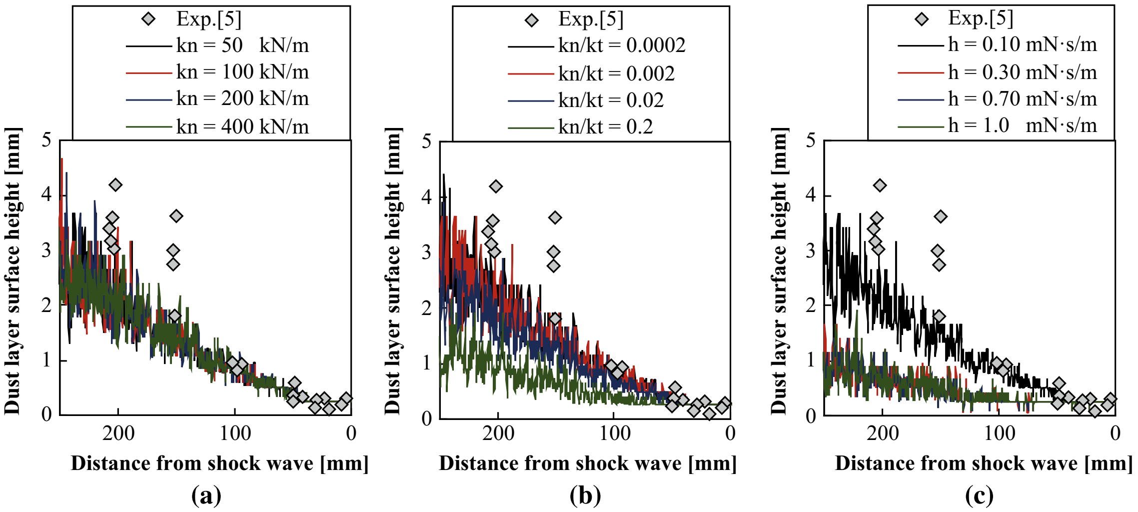

Fig. 5 Horizontal dust layer surface height distributions at 0.6 ms for different DEM parameters without the Magnus force. The dust layer surface was defined as $\alpha_p < 1.0 \times 10^{-4}$. **a** Spring constant, normal direction ($k_n/k_t = 0.002$, $h = 0.10$ mN s/m). **b** Spring constant, tangential direction ($k_n = 50$ kN, $h = 0.10$ mN s/m). **c** Damping constant, both directions ($k_n = 50$ kN, $k_n/k_t = 0.002$)

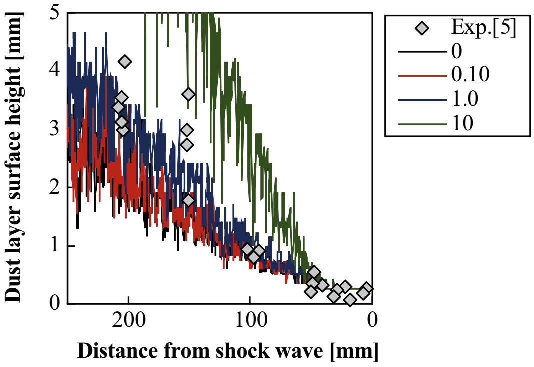

Fig. 6 Horizontal dust layer surface height distributions at 0.6 ms for different Magnus force constants C_{LM}. The dust layer surface was defined as $\alpha_p < 1.0 \times 10^{-4}$

3.3 Shock wave geometry and flow field

Figure 8 shows the evolution of the gas pressure and parcel distributions over time, with the black dots indicating the parcel positions. The shock wave propagates from left to right and is curved by interaction with the particle layer, as shown in Fig. 8b at $t = 0.1$ ms. The particles start to rise $t = 0.5$–1.0 ms after the shock wave propagates, as shown in Fig. 8b, c. Near this point (at $0 < x < 20$ mm), the particle dispersion is higher than elsewhere, because the shock wave diffracts and compresses the layered particles directly. Interaction between the shock-induced flow and dispersed dust at $x = 20$ mm causes the gas pressure to increase at $x = 10$–20 mm and decrease at 20–40 mm, as shown in Fig. 8d.

Figure 9 shows the geometries of the shock wave and dust layer at 0.5 ms. The gas pressure distribution (Fig. 9a) shows that the shock wave is curved above the dust layer and oblique inside it, due to the different shock propagation velocities in these regions. The wave's attenuation causes the speed of sound in the gas–particle mixture to become slower than in the pure fluid. This calculation does not treat the speed of sound in the gas–particle mixture specially, and in the gas phase, it was explicitly calculated as $c_g^2 = \gamma_g R_g T_g$ over the whole region. The shock wave's geometry and propagation velocity are affected by the phase interaction term in (1–3), and its velocity decreases inside the dust layer. The effective speed of sound through the particle phase appears implicitly as a result of the particles' rigid-body motion and collisions, as shown by the contact force distribution in Fig. 9b. The forces in front of the shock wave are small, indicating that the speed of the compaction wave in the particle phase is the same as that of the shock wave in the gas phase and that the particles start to move after the shock wave. The shock wave inside the dust layer is therefore slowed by interactions with stationary particles, and its direction then becomes oblique as it interacts with the faster shock wave in the pure gas region.

The shock-induced flow's gas velocity immediately decreases inside the dust layer when $x < 232$ mm, as shown by the gas velocity distribution in Fig. 9c. There are two reasons for this: momentum transfer between the gas and particles due to velocity differences, and compression waves generated by particle motion. The particles move right after the shock wave propagates and the particle layer's porosity decreases, leading to the gas phase being compressed. This particle motion thus generates compression waves. The pressure inside the dust layer increases continuously across the shock wave, as indicated in Fig. 9a, but this cannot be explained by momentum transfer between the gas and particles: if the gas phase's

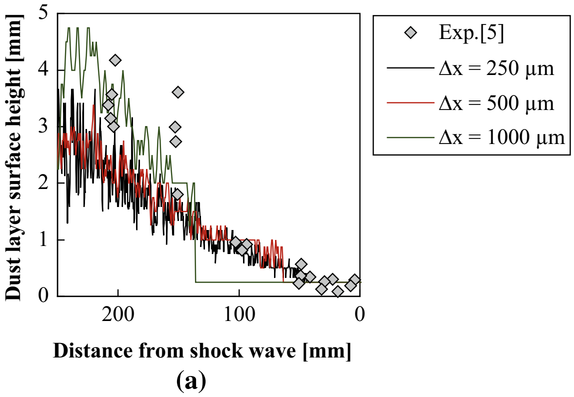

Fig. 7 Effect of the grid resolution and the parcel diameter on dust lifting height. The dust layer surface was defined as $\alpha_p < 1.0 \times 10^{-4}$. **a** Grid resolution (parcel diameter = 100 μm). **b** Parcel diameter (grid resolution = 500 μm)

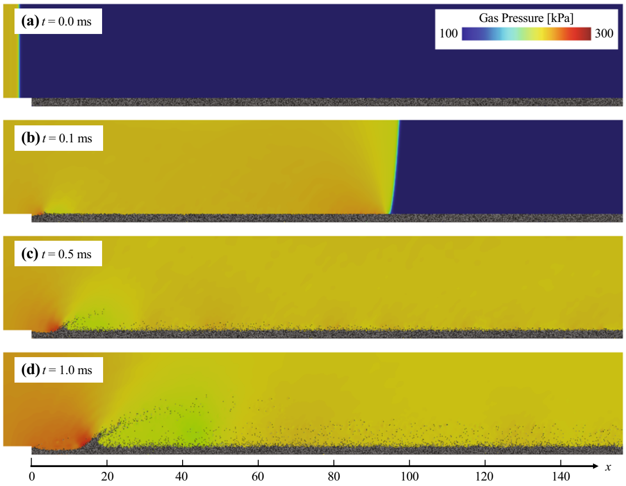

Fig. 8 Time evolution of the gas pressure field and parcel distribution for $0 < x < 150$

momentum was being completely absorbed by the momentum transfer, the pressure behind the shock wave would not increase. Therefore, this continuous pressure increase must be due to the propagation of compression waves generated by particle motion. These waves convert the dynamic pressure into static pressure behind the shock wave. A vertical gas velocity component arises in the shock-induced flow due to the oblique shock wave propagating inside the dust layer, as shown in Fig. 9d, causing the particles to move vertically and starting the dust lifting process.

3.4 Forces acting on the particles

Figure 10 shows the evolution of the vertical and horizontal components of the forces acting on a single particle over time. These plots were calculated by averaging over two groups of particles: the surface layer particles initially located between $-0.1 < y < 0.0$ mm and $100 < x < 200$ mm, and the particles in the middle of the dust layer located between $-1.1 < y < -0.9$ mm and $100 < x < 200$ mm. The horizontal region between $100 < x < 200$ mm was selected to avoid the effect of the abrupt flow changes at the edge of the particle layer. To show its time evolution, the contact force was treated specially: the contact forces shown were averaged over 0.01 ms because they were nearly instantaneous. Since the shock wave encountered each particle at a different time, this time was defined as $t = 0$ ms for the averaging process.

Figure 10a shows the vertical components of the forces acting on the surface particles. The passage of the shock wave immediately generates downward drag and pressure forces (within $0 < t < 0.01$ ms). After this, a large upward contact force appears at 0.01 ms. With a maximum strength of 80 μN, this is much stronger than the pressure (− 10 μN) or drag (− 20 μN). The particles then start to move upwards. An upward Magnus force also appears, but its magnitude is smaller than that of the contact force between $0 < t < 0.1$ ms, so it has little effect on the particle dispersion during the initial phase of dust lifting. After 0.1 ms, the contact force decreases rapidly as the particles rise, due to the low collision frequency, while the Magnus force decreases more gradually from a peak of 8 μN and thus becomes the dominant dust lifting force. Meanwhile, the drag force remains at − 2 μN, meaning that the particles' vertical velocity becomes increasingly uniform over time.

Figure 10b shows the vertical components of the forces acting on the particles in the middle of the dust layer. These particles experience larger instantaneous pressure forces (− 18 μN) than the surface particles and feel upward contact forces earlier (at $0 < t < 0.05$ ms). The larger vertical pressure force is due to the shock wave traveling at a more oblique angle inside the dust layer (as shown in Fig. 9) and an increased downward drag force. The maximum upward contact force (47 μN) is less than that for the surface particles (80 μN), but it should be noted that the contact forces

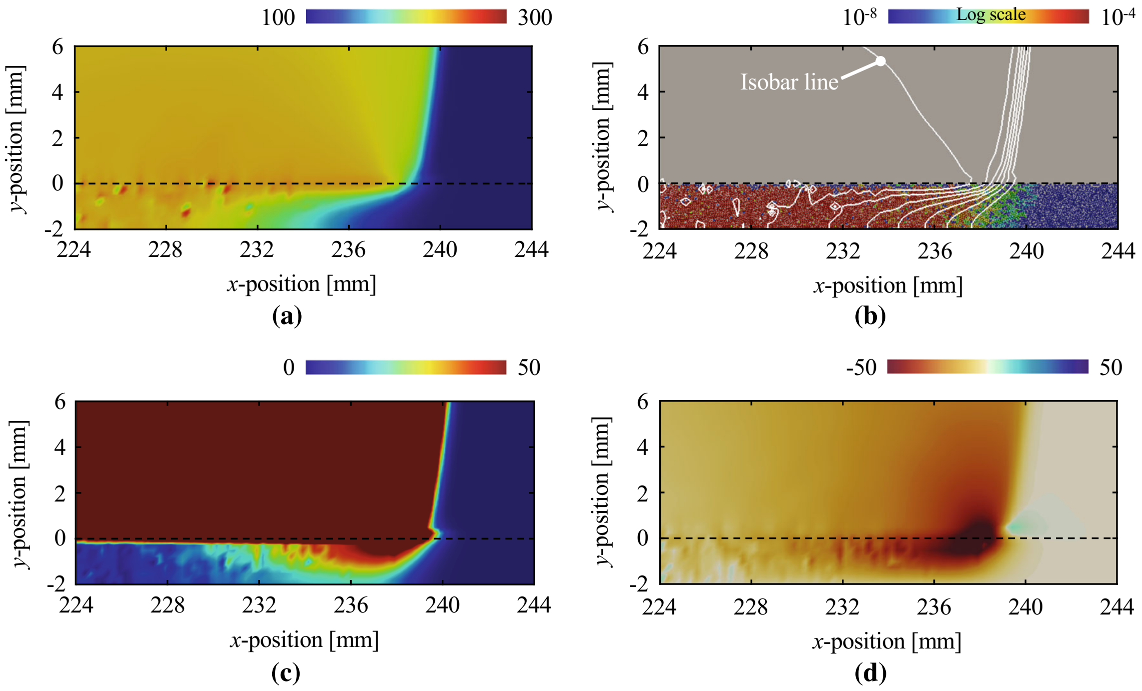

Fig. 9 Magnified view of the shock wave geometry at 0.5 ms. The region between $-2 < y < 0$ mm is inside the dust layer

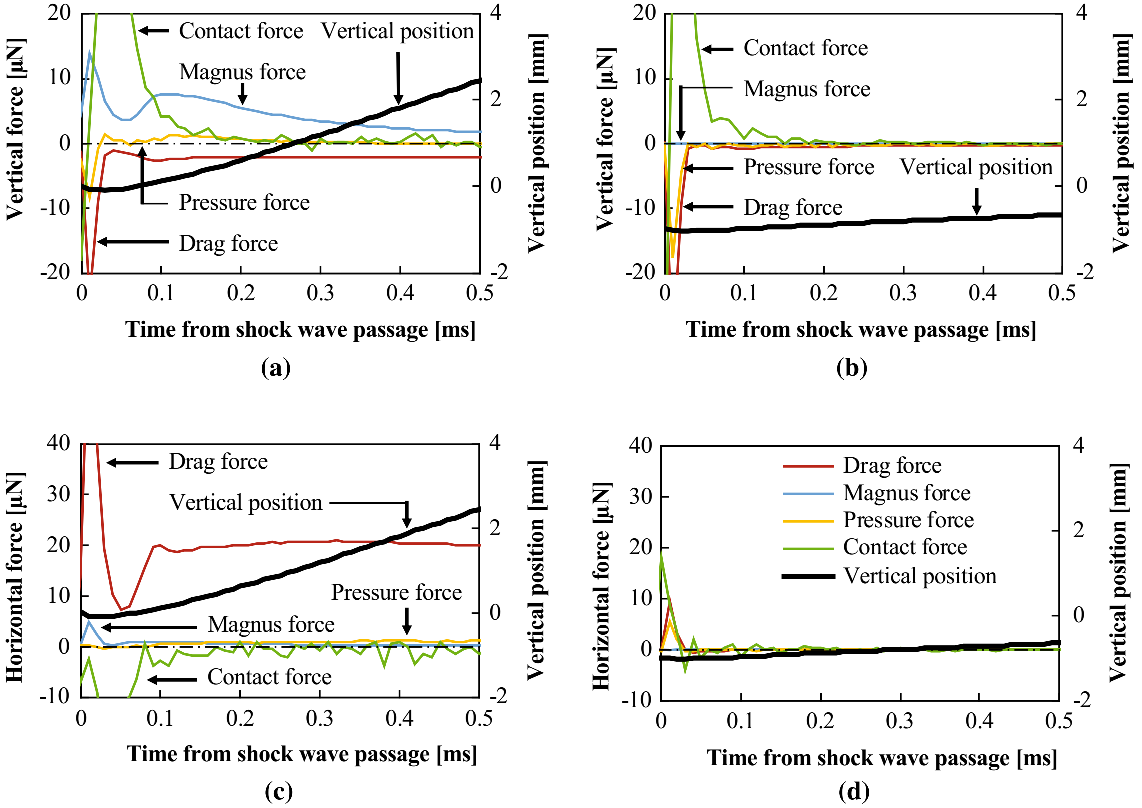

Fig. 10 Evolution of the vertical and horizontal components of the average force acting on a single particle for various initial vertical particle positions. The particles between $100 < x < 200$ mm were only included in the average in order to eliminate the effect of the abrupt flow change at the edge of the particle layer. The bold black line indicates the average dust particle height. **a** Vertical force at dust layer surface ($-0.1 < y < 0.0$ mm) maximum contact force = 80 μN. **b** Vertical force at middle of dust layer ($-1.1 < y < -0.9$ mm) maximum contact force = 47 μN. **c** Horizontal force at dust layer surface ($-0.1 < y < 0.0$ mm). **d** Horizontal force at middle of dust layer ($-1.1 < y < -0.9$ mm)

shown represent the sums of the upward and downward contact forces, so small values do not necessarily mean that the absolute force values are small. The upward contact force on the surface particles generates an opposite contact force on the lower particles, so the smaller contact forces shown in Fig. 10b are due to downward contact forces from the surface particles. The internal particles are therefore prevented from moving vertically by the surface particles. No vertical forces act on the particles after 0.1 ms because the gas phase has stopped moving.

Figure 10c, d shows the evolution of the horizontal forces on the (c) surface and (d) internal particles, with positive values indicating rightward forces. According to Fig. 10c, the horizontal forces consist of a rightward drag force and a leftward contact force. Before the shock wave passes ($t < 0.1$ ms), the particles are accelerated rightwards due to interaction with the shock-induced flow but are also decelerated by collisions with the particles ahead of them. After 0.1 ms, the contact force rapidly decreases, while the drag force remains constant, so the particles continue to be accelerated. In the internal region, all the forces act rightwards, as shown in Fig. 10d, meaning that all the particles in this region move rightward.

Figure 11 illustrates the dust lifting mechanism indicated by these results. First, drag and pressure forces act downwards after the oblique shock wave has propagated, causing the particles in the dust layer to move downwards and be pressed against the bottom floor. This causes a strong upward contact force and the particles start to rise. The contact force then decreases rapidly due to the low collision frequency in the dispersed medium. Finally, the Magnus force becomes dominant and the particles maintain their upward movement.

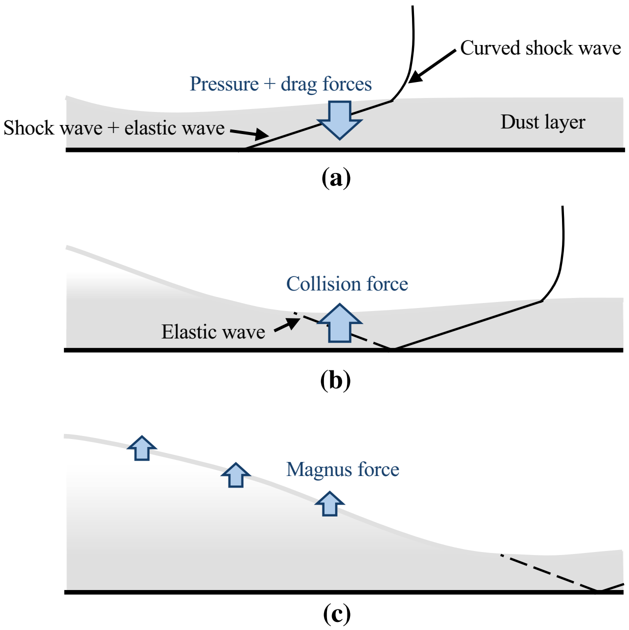

Fig. 11 Dust lifting mechanism indicated by the simulation results ($M_\mathrm{s} = 1.44$, particle diameter = 100 m, depth of the dust layer = 2 mm). **a** Pressure and drag forces act downwards immediately after the shock wave passes. **b** An upward collision force appears, and the dust particles start to rise. **c** The collision force rapidly decreases after the upward motion begins and the Magnus force becomes dominant

Figure 12 shows the time evolution of the (a) Magnus force $\mathbf{F}_{\mathrm{Magnus}}$, (b) relative rotation ω_r, (c) particle rotation ω_p, and (d) gas rotation Ω_g, for the same surface particles as were considered for Fig. 12a, c. The gray scatter plots show the data for individual particles, while the red lines show the averages. The relative rotation, $\omega_\mathrm{r} = \Omega_\mathrm{g} - \omega_\mathrm{p}$, is the instantaneous relative angular velocity used to evaluate the Magnus force. According to Fig. 12a, b, there is a downward trend in the Magnus force after 0.1 ms, due to the decreased relative rotation. Figure 12c, d shows that the gas rotation is 50 times larger than the particle rotation and hence that the Magnus force is driven by the gas rotation. The particle rotation is positive, reducing the relative rotation and hence the Magnus force, due to the contribution of the gas–particle interaction $\mathbf{M}_{\mathrm{rotation}}$. This can be concluded because the particle rotation increases gradually over a long period, while the particle–particle interaction $\mathbf{M}_{\mathrm{contact}}$ is an almost instantaneous torque. If $\mathbf{M}_{\mathrm{contact}}$ was dominant, the particle rotation would change discontinuously. In contrast, the torque from the gas–particle interactions acts to reduce the angular velocity difference between the gas and particles, causing the particle rotation to become positive.

To confirm the gas rotation behind the shock wave, Fig. 13 shows the (a) horizontal gas velocity and (b) gas vorticity distributions. From Fig. 13a, the gas velocity decreases in the region of dispersed particles above the dust layer due to the aerodynamic forces, and then, a positive horizontal velocity gradient ($\partial u_\mathrm{g}/\partial y > 0$) is generated. In addition, the curved shock wave causes the gas velocity to be vertically downward outside the dust layer, as shown in Fig. 9d, decreasing as it impinges on the layer's surface. Thus, the vertical velocity gradient is negative above the layer ($\partial v_\mathrm{g}/\partial x < 0$). Combining these results shows that the gas rotation above the dust layer is positive, $\Omega_\mathrm{g} = 2 \times (\partial u_\mathrm{g}/\partial y - \partial v_\mathrm{g}/\partial x) > 0$, as shown in Fig. 13b. The main factor driving the Magnus force is therefore the velocity gradient above the dust layer, induced by the interaction with the shock-induced flow. Figure 12d shows that the gas rotation decreases over time. The region where there is a velocity gradient becomes thicker and smaller over time, because the region of dispersed particles becomes wider and thinner. This reduction in the gas rotation is therefore due to the progressive particle dispersion. The Magnus force thus becomes insignificant.

Figure 13c shows how the Magnus force is generated. The mechanism for the shock dispersion process is different than for ordinary Magnus forces. Ordinary Magnus forces are driven by particle rotation, which generates an asymmet-

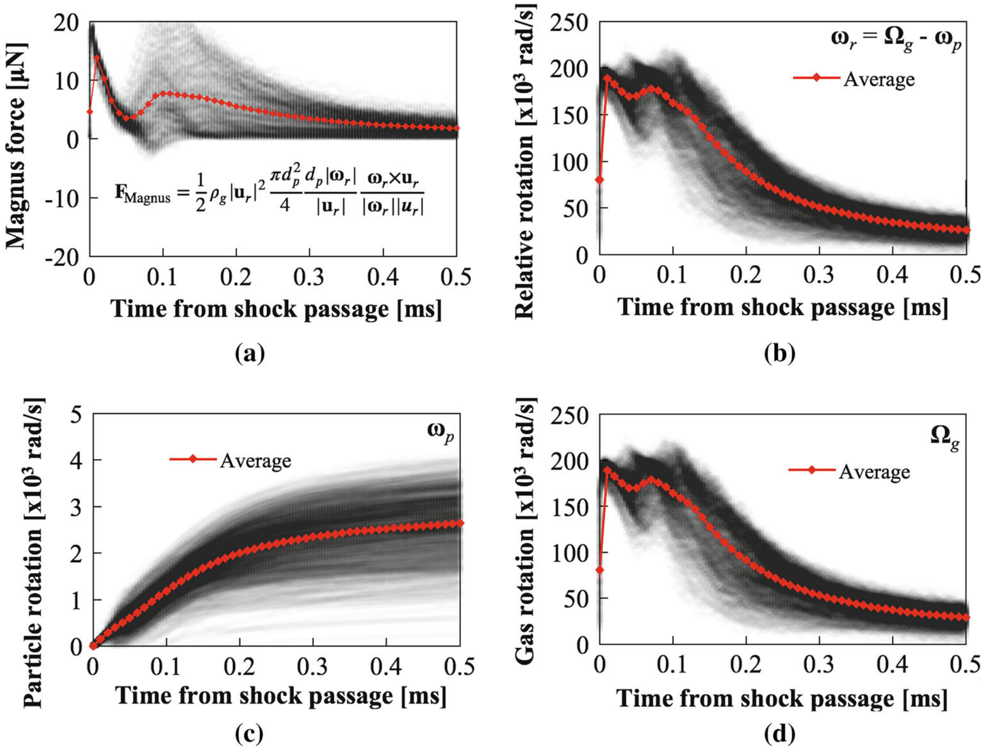

Fig. 12 Time evolution of the particle variables used to estimate the Magnus force. The particles between $100 < x < 200$ mm were only used to plot the time evolution and calculate the average values. **a** Magnus force. **b** Relative rotation. **c** Particle rotation. **d** Gas Rotation

ric gas velocity field in the vertical direction and hence an asymmetric gas pressure field. The force then acts vertically on the particles. For ordinary Magnus forces, there is a delay after the particle rotation begins before the vertical force is generated. In contrast, the Magnus force for the shock dispersion process is generated by the gas vorticity above the dust layer. In this case, the force appears immediately after the gas vorticity is generated, and occurs just behind the shock wave as it propagates along the dust layer.

4 Conclusion

This paper has used the CFD–DEM to simulate particle dispersion by vertical shock waves. The simulation results were compared with those of a previous experimental study [5], showing that the predictions were in good agreement in terms of the particle motion and shock wave geometry. The forces acting on individual particles have also been analyzed to investigate the dust dispersion mechanism.

The shock wave and dust layer geometries were similar to those found by previous simulations that used an Eulerian–Eulerian approach [12]. The shock wave was curved above the dust layer and oblique inside it, due to the different speeds of sound in these regions. The oblique shock wave generated a vertical gas velocity component in the shock-induced flow and caused the dust layer particles to move vertically. The interaction between the shock wave and the dust generated compression waves, the propagation of which caused the gas pressure inside the layer to increase continuously and the corresponding gas velocity to decrease behind the shock wave.

The drag and pressure forces initially acted downwards after the shock wave passed, compressing the particles against the bottom wall. This compression resulted in a strong upward contact force, and the dust particles started to rise. The Magnus force also acted upwards, but its magnitude was lower than that of the contact force. After the dust started to rise, the contact force decreased rapidly, due to the lower particle collision frequency, meaning that the Magnus force became dominant and the particles maintained their upward movement. Although the drag force acted downwards, its magnitude was lower and it could not prevent the Magnus force from continuing to push the particles upwards. However, the Magnus force gradually decreased as the particles rose while the drag force was almost constant, meaning that the drag and Magnus forces eventually balanced.

The main factor driving the Magnus force was the gas rotation, as the particle rotation had little effect. The gas rotation was generated by gas–particle interactions in the particle dispersion region. The gas velocity gradient above

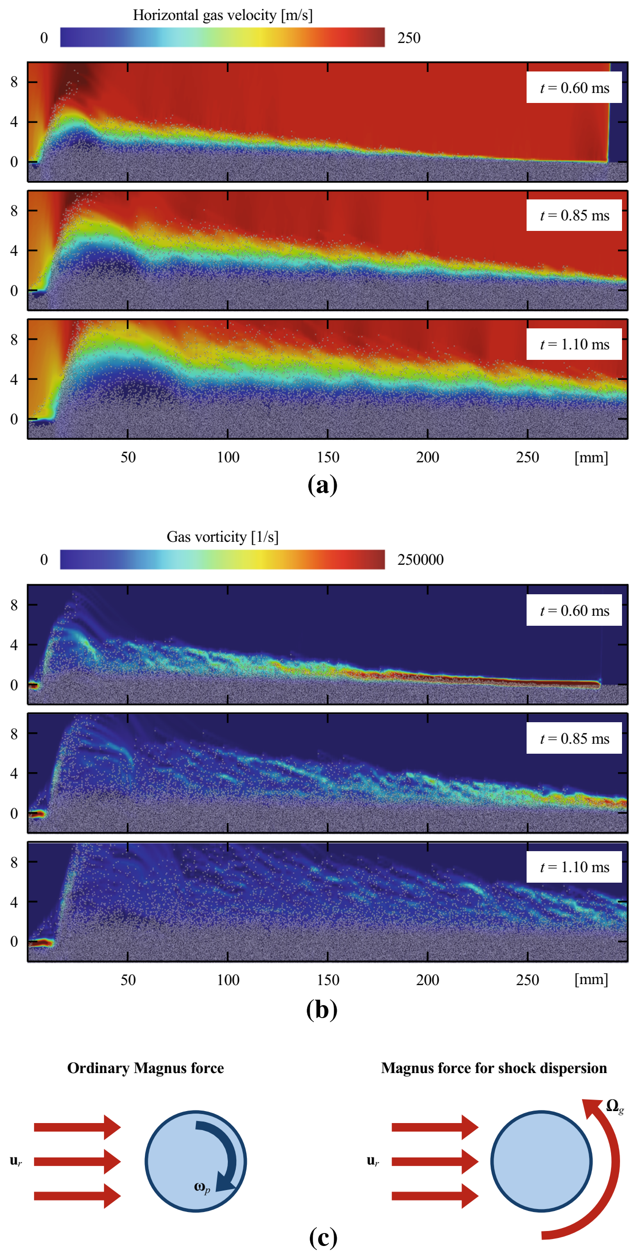

Fig. 13 Time evolution of the gas velocity field on the dust layer's surface. The velocity gradients above the dust layer is developed by the presence of dispersed particles. **a** Horizontal gas velocity distribution. **b** Gas vorticity distribution. **c** Magnus force generation mechanisms

the dust layer became smaller over time, because the particle dispersion region became wider and thinner, so the Magnus force decreased after the shock wave passed (after 0.1 ms). The main factor driving the drag force was the velocity difference between the particles and the ambient gas. In shock-induced flows, the drag force remains constant but the Magnus force decreases as long as the particles are in uniform vertical motion, leading the Magnus force to eventually become insignificant and allowing the drag force to stop the particles rising.

Acknowledgements This work was supported by JSPS KAKENHI Grant Number JP18H01387. This work was supported by "Joint Usage/Research Center for Interdisciplinary Large-scale Information Infrastructures" and "High Performance Computing Infrastructure" in Japan. (Project ID: jh160020, hp160183, jh170040, and hp170039). Part of the simulated results in this research was obtained using the supercomputing resources at Cyberscience Center, Tohoku University, Japan.

References

1. Yuan, Z., Khakzad, N., Khan, F., Amyotte, P.: Dust explosions: A threat to the process industries. Process Saf. Environ. Prot. **98**, 57–71 (2015). https://doi.org/10.1016/j.psep.2015.06.008
2. Dawes, J.G.: Safety in Mine Research Establishment. Ministry of Fuel and Power, UK (1952)
3. Gerrard, J.H.: An experimental investigation of the initial stages of dispersion of dust by shock waves. Br. J. Appl. Phys. **14**, 186–192 (1963). https://doi.org/10.1088/0508-3443/14/4/306
4. Fletcher, B.J.: Interaction of a shock with a dust deposit. J. Phys. D Appl. Phys. **9**, 197–202 (1976). https://doi.org/10.1088/0022-3727/9/2/009
5. Suzuki, T., Adachi, T.: The effects of particles size on shock wave-dust deposit interaction. Proceedings of the 14th International Symposium on Space Technology Science, Tokyo, Japan (1984)
6. Chowdhury, A.Y., Marks, B.D., Johnston, H.G., Mannan, M.S., Peterson, E.L.: A new facility for studying shock-wave passage over dust layers. Shock Waves **26**, 129–140 (2016). https://doi.org/10.1007/s00193-015-0586-z
7. van der Hoef, M.A., van Sint Annaland, M., Deen, N.G., Kuipers, J.A.M.: Numerical simulation of dense gas-solid fluidized beds: A multiscale modeling strategy. Annu. Rev. Fluid Mech. **40**, 47–70 (2008). https://doi.org/10.1146/annurev.fluid.40.111406.102130
8. Gidaspow, D.: Multiphase Flow and Fluidization: Continuum and Kinetic Theory Descriptions. Academic Press, Boston (1994). https://doi.org/10.1002/aic.690420438
9. Houim, R.W., Oran, E.S.: Structure and flame speed of dilute and dense layered coal-dust explosions. J. Loss Prev. Process Ind. **36**, 214–222 (2015). https://doi.org/10.1016/j.jlp.2015.01.015
10. Houim, R.W., Oran, E.S.: A multiphase model for compressible granular–gaseous flows: formulation and initial testes. J. Fluid Mech. **789**, 166–220 (2016). https://doi.org/10.1017/jfm.2015.728
11. Ugarte, O.J., Houim, R.W., Oran, E.S.: Examination of the forces controlling dust dispersion by shock waves. Phys. Rev. Fluid **2**, 074304 (2017). https://doi.org/10.1103/PhysRevFluids.2.074304
12. Khmel, T.A., Fedorov, A.V.: Effect of collision dynamics of particles on the processes of shock wave dispersion. Combust. Explos. Shock Waves **52**, 207–218 (2016). https://doi.org/10.1134/S0010508216020118
13. Ishii, M., Hibiki, T.: Thermo-Fluid Dynamics of Two-Phase Flow. Springer, New York (2011). https://doi.org/10.1007/978-1-4419-7985-8
14. McBride, B., Gordon, S., Reno, M.A.: Coefficient for calculating thermodynamic and transport properties of individual species. NASA Tech. Memo. 4513 (1993)
15. Gordon, S., McBride, B., Zeleznik, F.J.: Computer program for calculation of complex chemical equilibrium compositions and applications. Supplement 1—Transport properties. NASA Tech. Memo. 86885 (1984)

16. Theofanous, T., Chan, C.: The dynamics of dense particle clouds subjected to shock waves. Part 2. Modeling/numerical issues and the way forward. Int. J. Multiph. Flow **89**, 177–206 (2017). https://doi.org/10.1016/j.ijmultiphaseflow.2016.10.004
17. Ranz, W.E., Marshall, W.R.: Evaporation from drops. Chem. Eng. Prog. **48**, 141–146 (1952)
18. Ling, Y., Wagner, J.L., Beresh, S.J., Kearney, S.P., Balachandar, S.: Interaction of a planar shock wave with a dense particle curtain: Modeling and experiments. Phys. Fluids **24**, 113301 (2012). https://doi.org/10.1063/1.4768815
19. Parmar, M., Haselbacher, A., Balachandar, S.: Improved drag correlation for spheres and application to shock-tube experiments. AIAA J. **48**, 1273–1276 (2010). https://doi.org/10.2514/1.J050161
20. Sangani, A.S., Zhang, D.Z., Prosperetti, A.: The added mass, Basset, and viscous drag coefficients in nondilute bubbly liquids undergoing small-amplitude oscillatory motion. Phys. Fluids A **3**, 2955 (1991). https://doi.org/10.1063/1.857838
21. Lun, C.K.K., Liu, J.S.: Numerical simulation of dilute turbulent gas-solid flows in horizontal channels. Int. J. Multiph. Flow **23**, 575–605 (1997). https://doi.org/10.1016/S0301-9322(96)00087-0
22. Dennis, S.C.R., Singh, S.N., Ingham, D.B.: The steady flow due to a rotating sphere at low and moderate Reynolds numbers. J. Fluid Mech. **101**, 257–279 (1980). https://doi.org/10.1017/S0022112080001656
23. Sakai, M., Abe, M., Shigeto, Y., Takahashi, H., Vire, A., Percival, J., Xiang, J., Pain, C.: Verification and validation of coarse grain model of the DEM in a bubbling fluidized bed. Chem. Eng. J. **244**, 33–43 (2014). https://doi.org/10.1016/j.cej.2014.01.029
24. Kitamura, K., Shima, E.: Towards shock-stable and accurate hypersonic heating computations: A new pressure flux for AUSM-family schemes. J. Comput. Phys. **245**, 62–83 (2013). https://doi.org/10.1016/j.jcp.2013.02.046
25. Gottlieb, S., Shu, C., Tadmor, E.: Strong stability-preserving high-order time discretization methods. SIAM Rev. **43**, 89–112 (2001). https://doi.org/10.1137/S003614450036757X
26. Tsuji, Y., Morikawa, Y., Mizuno, O.: Experimental measurement of the Magnus force on a rotating sphere at low Reynolds numbers. J. Fluids Eng. **107**, 484–488 (1985). https://doi.org/10.1115/1.3242517
27. Oesterle, B., Dinh, B., Vial, J.L.: Measurements of lift and torque on a rotating sphere at intermediate Reynolds numbers. Mech. Res. Commun. **18**, 145–150 (1991). https://doi.org/10.1016/0093-6413(91)90043-V